Identifying open-orbit topological surface states in dual topological semimetal $TaSb_2$

Susmita Changdar,[1,2,*] Heike Schlörb,[1] Oleksandr Suvorov,[1] Dmitri V. Efremov,[1] Alexander Yaresko,[3] Rui Lou,[1,4] Alexander Fedorov,[1,4] Bernd Büchner,[1] Andy Thomas,[1] Sergey Borisenko,[1,†] and Setti Thirupathaiah[2,‡]

[1]*Leibniz Institute for Solid State and Materials Research, IFW Dresden, 01069 Dresden, Germany*

[2]*Condensed Matter and Materials Physics Department, S. N. Bose National Centre for Basic Sciences, Kolkata, West Bengal-700106, India*

[3]*Max Planck Institute for Solid State Research, Heisenbergstrasse 1, 70569 Stuttgart, Germany*

[4]*Helmholtz-Zentrum Berlin für Materialien und Energie, Elektronenspeicherring BESSY II, 12489 Berlin, Germany*

(Received 16 February 2026; accepted 24 July 2026; published 20 August 2026)

$TaSb_2$, a member of the $TmPn_2$ family of materials, hosts the very rare dual topological phase—weak topological insulating state and topological crystalline insulating state along different crystallographic orientations. So far, studies on the electronic structure of $TmPn_2$ compounds have focused on their overall electronic structure and the bulk open-orbit Fermi surfaces. Using angle-resolved photoemission spectroscopy, density functional theory calculations, and transport measurements, we distinguish the intertwined bulk and surface states on the weakly topological $(20\bar{1})$ plane of $TaSb_2$. We identify multiple electron- and holelike bulk bands, yielding a near-perfect carrier compensation. Crucially, we observe open-orbit FSs near $\bar{M}$ and parallel to $\bar{\Gamma}-\bar{Y}$ direction that are entirely of surface origin. The surface states also exhibit band crossing at ∼0.6 eV below Fermi level at the time-reversal invariant momentum $\bar{M}$, indicating nontrivial band topology. Consistent with this, magnetotransport measurements display weak antilocalization, establishing $TaSb_2$ as a platform for spin-polarized topological transport on a weakly topological surface.

DOI: 10.1103/9gk1-krjp

I. INTRODUCTION

Since the discovery of the quantum Hall effect [1], the interest in realizing nontrivial band topology in various materials has grown significantly. Over the years, this field has expanded from quantum Hall effect to topological insulators (TIs) [2–5], Dirac [6–8] and Weyl semimetals [9–12], topological superconductors [13–15], and the other classifications of topological materials [16–18]. The surface/edge states in these materials are spin-momentum locked and protected by symmetries, making them robust against disorder and promising for applications in spintronics and quantum computing [19,20]. Followed by the discovery of Weyl semimetallic phase and Fermi arcs in transtion metal pnictides (TaAs, TaP, NbAs) [10,11,21,22], the transition metal dipnictides $TmPn_2$ (Tm=Ta, Nb, and Pn=P, As, Sb) attracted a lot of attention for hosting many fascinating properties including topologically nontrivial electronic states [23–29], giant Nerst thermopower [28,30], extremely large magnetoresistance (XMR) [31–37], negative MR [31,38,39], and superconductivity [40,41].

$TaSb_2$, a member of the $TmPn_2$ family, behaves as a nodal line semimetal in the absence of spin-orbit coupling (SOC). Due to band inversion, SOC opens a gap at the nodal line [23,25]. Based on the $\mathbb{Z}_2$ invariants $(\nu_0;\nu_1\nu_2\nu_3)$, $TaSb_2$ is a weak topological insulator (WTI) (0; 111) [23]. Strong topological insulators (STIs) are classified with strong topological invariant, $\nu_0 = 1$, whereas for WTIs, $\nu_0 = 0$ with one of the invariants $(\nu_1\nu_2\nu_3)$ being nonzero [42–44]. Based on these weak invariants, the surface states in WTIs are only protected on certain directions. Moreover, $TaSb_2$ has monoclinic crystal structure which hosts C_{2h} point group symmetry [25,45–47]. C_{2h} consists of mirror, rotational, and inversion symmetry. $TaSb_2$ hosts nontrivial surface states protected by rotational symmetry $C_{2(010)}$ along the (010) plane, making it a topological crystalline insulator (TCI) [25,47]. The coexistence of WTI and TCI states on different facets makes $TaSb_2$ particularly compelling. While similar coexisting topological phases have been observed in layered materials [48–50], their topologically relevant surfaces are difficult to access. In contrast, the intrinsically three-dimensional nature of $TaSb_2$ provides an ideal platform to directly probe and manipulate surface states protected by distinct symmetries, enabling exploration of rich underlying physics as well as potential applications in low-dissipation electronics and next-generation spintronic devices [51,52].

In this work, we investigate the bulk and surface electronic structure of $TaSb_2$ and their impact on magnetotransport properties. Using Angle-resolved photoemission spectroscopy (ARPES) alongside first-principles calculations, we identify topological surface states coexisting with bulk bands at the Fermi level. Magnetotransport measurements reveal pronounced anisotropy arising from the anisotropic Fermi surface (FS) of $TaSb_2$ and signatures of quantum interference effects

*Contact author: s.changdar@ifw-dresden.de
†Contact author: s.borisenko@ifw-dresden.de
‡Contact author: setti@bose.res.in

Published by the American Physical Society under the terms of the Creative Commons Attribution 4.0 International license. Further distribution of this work must maintain attribution to the author(s) and the published article's title, journal citation, and DOI.

linked to these surface states. Our results establish $TaSb_2$ as a compelling platform to study the interplay between distinct topological phases and transport phenomena.

II. EXPERIMENTAL DETAILS

Single crystals of $TaSb_2$ were grown by chemical vapor transport method. In this method, initially we prepare the pollycrystalline sample of $TaSb_2$. To prepare, a stoichiometric amount of Ta and Sb were thoroughly mixed together and kept in a vacuum sealed quartz ampule which was then heated at 650 °C for 12 hours and then at 750 °C for 72 hours in a muffle furnace. The obtained pollycrystalline $TaSb_2$ sample was then vacuum sealed in a quartz ampule (10^{-4} mbar) with iodine as the transport agent (iodine concentration: 10 gm/cc). The quartz ampule was then kept inside the gradient tube furnace for 14 days with the source and sink temperatures set at 1050 °C and 950 °C, respectively. The furnace was then cooled down to the room temperature. In this way, we obtained several single crystals of $TaSb_2$ with a typical size of 2×3 mm^2.

ARPES measurements on $TaSb_2$ were performed on the $(20\bar{1})$ plane. The experiments were carried out at 1^3 ARPES end station in BESSY-II (Helmholtz Zentrum Berlin) synchrotron radiation center. Measurements were performed with angular resolution of 0.2°. During the measurements, the sample temperature was kept at 1.5 K, and the photon energy was varied within the range of 30–100 eV. The overall energy resolution was within 10–15 meV. Throughout the measurements the chamber pressure was kept at 9×10^{-11} mBar.

Magnetotransport measurements on $TaSb_2$ single crystals were performed in an Oxford Instruments cryostat with a variable temperature insert (VTI) and a superconducting split coil magnet, which allows to apply external magnetic fields of up to 7 T. Moreover, the cryostat is equipped with a stepper motor rotation platform that allows the sample to rotate in the magnetic field in a fixed plane. The current was applied using a Keithley 2450 sourcemeter and both the longitudinal and transversal voltages were measured using Keithley 2182A nanovoltmeters.

III. COMPUTATIONAL DETAILS

First-principles calculations for $TaSb_2$ were performed within density functional theory using the full-potential local-orbital code FPLO [53,54]. Exchange and correlation were treated in the generalized gradient approximation (GGA) in the Perdew-Burke-Ernzerhof parametrization [55]. The Brillouin zone was sampled with a $12 \times 12 \times 12k$-point mesh, and spin-orbit coupling was treated within the full-relativistic mode of FPLO. The experimental lattice parameters of Refs. [56,57] were used.

To obtain the surface electronic structure, we constructed a tight-binding Hamiltonian from projective Wannier functions generated within FPLO, using projectors onto the Ta $5d$ and Sb $5p$ orbitals over an energy window of $[-5, 6]$ eV relative to the Fermi level. Surface states were then computed from the surface Green's function of a semi-infinite system using the iterative scheme of Sancho *et al.* [58], as implemented in the pyfplo module of FPLO. We considered the $(20\bar{1})$ surface, which is the natural cleavage plane, and the spectral function was evaluated for the Sb termination.

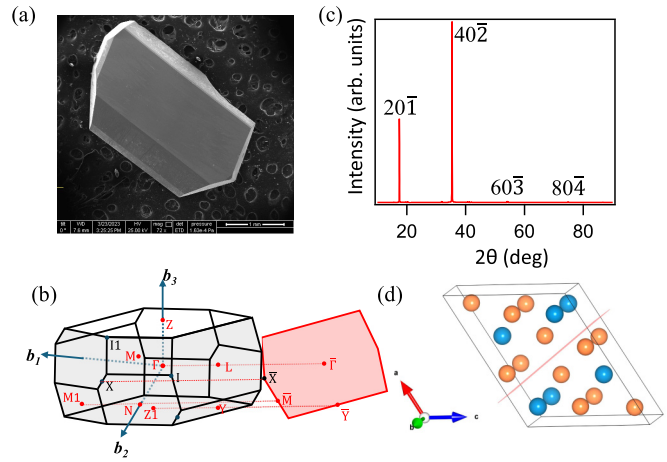


FIG. 1. Crystal structure of $TaSb_2$. (a) SEM image of the $TaSb_2$ single crystal. (b) The primitive BZ of $TaSb_2$ with the 2D BZ of the $(1\bar{1}\bar{1})$ plane. b_1, b_2, and b_3 are the reciprocal lattice vectors for the primitive unit cell. The high-symmetry points marked in red are time-reversal invariant momenta (TRIM). The $(1\bar{1}\bar{1})$ plane corresponds to the $(20\bar{1})$ plane for conventional unit cells [23]. (c) The XRD data collected from the $(20\bar{1})$ plane of $TaSb_2$. (d) Schematic of the conventional unit cell of $TaSb_2$ with the $(20\bar{1})$ plane. The blue atoms stand for Ta, and orange atoms are Sb.

Bulk band structure calculations were performed using PY LMTO [59] implementation of the linear muffin tin orbitals (LMTO) method. Spin-orbit coupling was added to the LMTO Hamiltonian at the variational step.

IV. RESULTS AND DISCUSSION

$TaSb_2$ crystallizes in a monoclinic structure with space group $C12/m1$. Scanning electron microscopy (SEM) image of a typical single crystal is shown in Fig. 1(a), displaying its well-faceted morphology. To define the ARPES measurement geometry, we present the three-dimensional Brillouin zone (BZ) of the primitive unit cell, along with its projection onto the $(1\bar{1}\bar{1})$ plane [equivalent to the $(20\bar{1})$ plane for conventional unit cell] in Fig. 1(b). The x-ray diffraction (XRD) data, shown in Fig. 1(c), confirm that the cleaved surface is indeed the $(20\bar{1})$ plane. Furthermore, we demonstrate the conventional unit cell of $TaSb_2$, highlighting the arrangement of Ta and Sb atoms along with the $(20\bar{1})$ cleavage plane. This visualization helps to establish the correspondence between real-space orientation and the measured momentum space, providing a good understanding of the structural framework for interpreting the surface electronic structure discussed below.

Figure 2(a) displays the in-plane FS map, constant energy contours at $E_F - 0.2$ eV and $E_F - 0.3$ eV, measured with p-polarized light at a photon energy of $h\nu = 70$ eV. The corresponding calculated bulk band structures shown in the lower panels reveal excellent agreement with experimental intensity distributions near L and Z, confirming the bulk origin of states in these high symmetry points. A 50 meV shift toward higher binding energy was applied to all of the calculated bands to

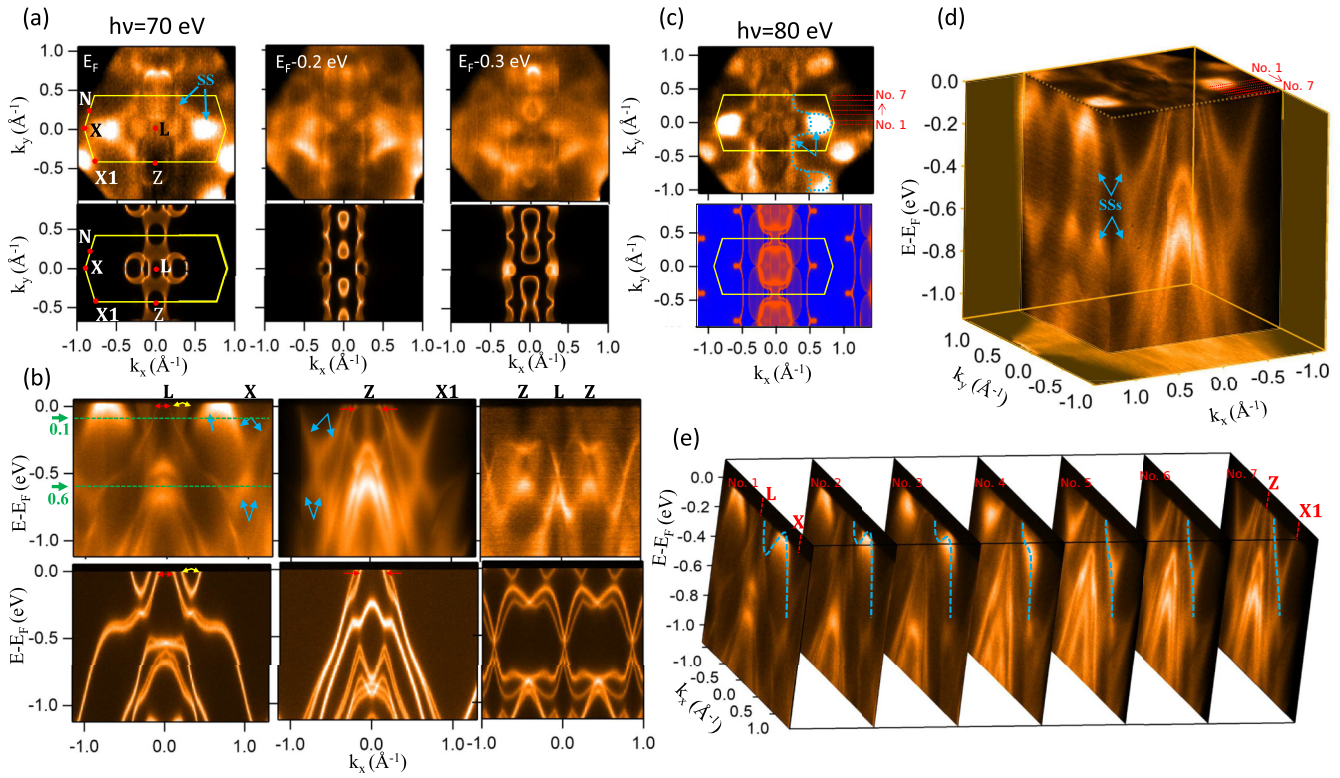


FIG. 2. In-plane electronic structure of $TaSb_2$. (a) Top: FS map (left) and constant energy contours at 0.2 eV (middle) and 0.3 eV (right) below the Fermi level from ARPES ($h\nu = 70$ eV). Bottom: corresponding bulk band calculations. (b) Top: EDMs along $L - X$ (left), $Z - X1$ (middle), and $L - Z$ (right). Bottom: corresponding bulk calculations. Blue arrows point the surface states. Green lines (top left panel) show the momentum distribution curve (MDC) used in the out-of-plane contours in Fig. 3(a). (c) FS map from ARPES (top) compared with surface state calculations (bottom). (d) 3D ARPES spectra showing the in-plane dispersion of the marked surface state. (e) Evolution of the band structure from $L - X$ toward $Z - X1$. Red dotted lines in (c) and (d) mark the positions of the EDM cuts.

align them with experimental Fermi level positions. We focus on the FS centered at L—located at $k_z = \pi$—rather than at Γ, where no spectral weight is present. Focusing on the ARPES spectra in Fig. 2(a), we observe a ripplelike, open-orbit structure near X. This feature is absent in bulk band calculations but emerges clearly in the semi-infinite slab calculations [bottom panel in Fig. 2(c)], confirming its surface origin.

Figure 2(b) presents energy-momentum dispersions (EDMs) along high-symmetry directions, with corresponding DFT results shown below each panel. These comparisons enable a clear distinction between bulk and surface-derived states (the latter highlighted by blue arrows). Along $L - Z$, the experimental bands align well with bulk calculations, reinforcing their bulk origin. Several dispersive bands crossing the Fermi level give rise to both electron and hole pockets, consistent with a semimetallic electronic structure. Along $L - X$, both electronlike (marked with yellow arrows) and holelike dispersions (marked with red arrows) are observed. In Fig. 2(c), we compare the FS map with DFT slab calculations. The momentum-space trajectory of the surface band is highlighted with blue dashed lines and is generally consistent with the calculated FS map, which reflects a surface closer to the (100) plane. As a result, the calculated surface states are less dispersive compared to the ARPES results. To visualize the surface-state dispersion across the Brillouin zone, Fig. 2(d) shows a 3D ARPES intensity map. Both ARPES and slab calculations in Fig. 2(c) reveal that the surface band crosses the Fermi level once along $Z - X1$, but twice along $L - X$. To elucidate this, EDMs along paths No. 1– No. 7 [Fig. 2(e)] are plotted. The dotted lines are a guide for the eye to show how the band dispersion evolves from an electronlike dispersion near $Z - X1$ to a mixed electron–hole-like character near $L - X$.

To showcase that the bands labeled as surface states in Fig. 2 have minimal k_z warping, we plotted the out-of-plane FS map, and the constant energy contours at $E_F - 0.1$ eV and $E_F - 0.6$ eV [Fig. 3(a)]. The inner potential used for calculating the k_z is $V_0 = 10$ eV. We have located the L, Γ, and L points at photon energies of 34 eV, 52 eV, and 70 eV, respectively [Fig. 3(a)]. Given an interplanar spacing $d = 5.06$ Å, these points correspond to $k_z \approx 5\pi/d$, $6\pi/d$, and $7\pi/d$ respectively. The contours showcase minimal k_z warping for the previously marked surface bands in the EDM along $L - X$ [top left panel in Fig. 2(b)], therefore reinforcing our assumption that they are k_z-independent surface states. Looking further into the k_z-independent surface states at $E_F - 0.6$ eV, we identify a surface band crossing at the TRIM $\bar{M}$ point (Fig. S2 in the Supplemental Material [60]). By calculating the Z_2 invariant, we find that the observed $(20\bar{1})$ plane is topologically nontrivial ($\nu = 1$) (Sec. I in the Supplemental Material [60]) and the band crossing is therefore consistent with the Dirac surface state expected in WTI phase [61–63]. Next we present the out-of-plane EDM. EDM taken at $k_x = k_y = 0$ Å^{-1} show that the dispersive band touches the Fermi

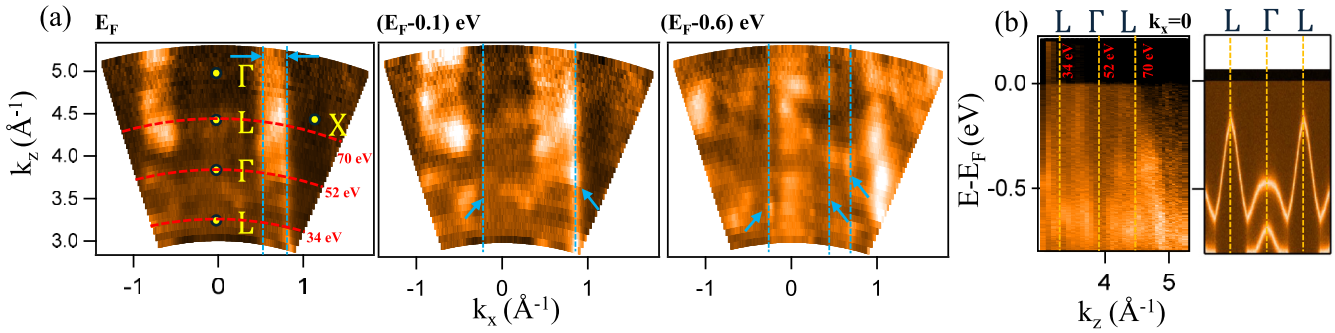


FIG. 3. Out-of-plane electronic structure. (a) Out-of-plane FS, constant energy contours acquired at 0.1 eV and 0.6 eV below the Fermi level, respectively. The blue dotted lines indicate the surface states exhibiting negligible k_z warping. (b) Left panel: Out-of-plane EDM obtained at $k_x = 0\,\text{Å}^{-1}$. Right panel: Corresponding bulk calculation.

level at 70 eV and at around 34 eV. Since, band dispersion along $\Gamma - L$ only crosses the Fermi level at L, with no bands near Γ [Fig. 3(b)], we mark the $h\nu = 70\,\text{eV}$ as a L point, and $h\nu = 52\,\text{eV}$ as a Γ point. The high symmetry points in the contour maps in Fig. 3(a) are mainly determined from here. The consideration is also quite in agreement with our consideration of the high symmetry points in Fig. 2.

We also performed comprehensive magnetotransport measurements to directly investigate the effect of both surface and bulk states on the transport properties of $TaSb_2$. The semimetallic nature of the sample reflects in the resistivity $\rho_{xx}(T)$ data from the $(20\bar{1})$ plane. We observed large positive magnetoresistance $[\text{MR} = [\rho_{xx}(B) - \rho_{xx}(0)]/\rho_{xx}(0)]$, reaching 1450% at 5 K and 7 T with an almost parabolic field dependence, which is suppressed upon increasing temperature. Consistent with the low-symmetry monoclinic crystal structure [35,64] and a complex FS [65], the MR is highly anisotropic [Fig. 4(c)]. We observe twofold rotational symmetry with a minimum for the I||B||b axis for in-plane rotation of the magnetic field. This is due to the effect of Lorentz force on the pockets maximizing when the field is perpendicular to the current direction. However, in the bottom panel of Fig. 4(c), the field always remains perpendicular to the current direction (I||b axis) and the maximum MR occurs when B is perpendicular to both the sample surface and the current direction ($\theta = 0°$). Here, $\text{MR}(B, \theta)$ reveals a clear deviation from parabolic field dependence with increasing θ [Fig. 4(d)]. The deviation becomes prominent above $\theta = 73°$. As the direction of the applied magnetic field changes, the effective cross section of the highly anisotropic electron- and hole-type Fermi pockets perpendicular to the field is modified, which in turn alters the transport contributions of electron and hole carriers in $TaSb_2$. A similar sensitivity of the $\text{MR}(B)$ curvature to effective carrier imbalance was demonstrated through simulations in the related compound ZrP_2 [66], where deviations from perfect electron-hole compensation led to a comparable deviation from the parabolic MR(B) curve.

For the out-of-plane field rotation with the rotation plane parallel to the current [Fig. 4(e)], the longitudinal magnetoresistance (LMR, $I \parallel B$ at $\theta = 90°$) exhibits an initial increase up to ~3 T before transitioning into a negative slope at higher fields. This low-field cusp is a signature of weak antilocalization (WAL), previously observed in isostructural $TaSb_2$ [31] and $TaAs_2$ nanowires [67], where it was attributed to the topological surface states. Therefore, the topological surface states we have identified by ARPES dominate the low-field transport near the in-plane orientation. At higher fields, the onset of negative LMR indicates crossover to a transport regime influenced by the chiral anomaly. Similar transitions from WAL-induced positive MR to chiral anomaly driven negative MR have been reported in several topological materials, including TaAs [68], $MoGe_2$ [69], and $PtSe_2$ [70]. The extreme angular sensitivity of the effect, with the negative MR component disappearing when the magnetic field is tilted by only 5° away from the longitudinal configuration ($\theta = 85°$), is consistent with a transport mechanism that depends on a finite $\mathbf{E} \cdot \mathbf{B}$ term, which is required for the suppression of backscattering between Weyl/Dirac nodes.

Moreover, the Hall measurements [Fig. 4(f)] confirmed the multiband nature and overall electron-dominated transport. A simultaneous two-band fitting of the conductivity tensors σ_{xx} and σ_{xy} using the standard formulas $\sigma_{xx} = \sum_{i=1}^{2} \frac{en_i\mu_i}{1+\mu_i^2B^2}$ and $\sigma_{xy} = \sum_{i=1}^{2} S_i \frac{en_i\mu_i^2B}{1+\mu_i^2B^2}$ (where $S_i = \pm 1$ for holes/electrons) yielded a near-perfect electron-hole compensation at 5 K, with electron carrier density $n_e = 2.78(1) \times 10^{20}\,\text{cm}^{-3}$ and mobility $\mu_e = 5.66(3) \times 10^3\,\text{cm}^2/\text{Vs}$, slightly exceeding the hole values ($n_h = 2.56(2) \times 10^{20}\,\text{cm}^{-3}$, $\mu_h = 3.45(3) \times 10^3\,\text{cm}^2/\text{Vs}$). This near perfect electron-hole compensation agrees with the ARPES results where we see both electron- and holelike bands, and is a strong contributor to the large MR [71] we observe. Overall, these transport results demonstrate that both topological surface states and the bulk electronic structure play crucial roles in determining the low-temperature electrical properties of $TaSb_2$.

Although we were unable to directly investigate the interplay between the surface states of the TCI and weak TI phases in $TaSb_2$, as the sample could not be cleaved along the (010) plane, future studies in this direction may provide valuable insights. Though the electronic and transport properties of $TaSb_2$ [29,31,35] have been previously investigated, in this work, we successfully isolated the topological surface states from the bulk, and their impact in transport. To date, experimental reports on the electronic structure of these materials remain scarce despite their fascinating topological properties. The three-dimensional nature of $TmPn_2$ compounds makes obtaining the high-quality cleaves required for ARPES excep-

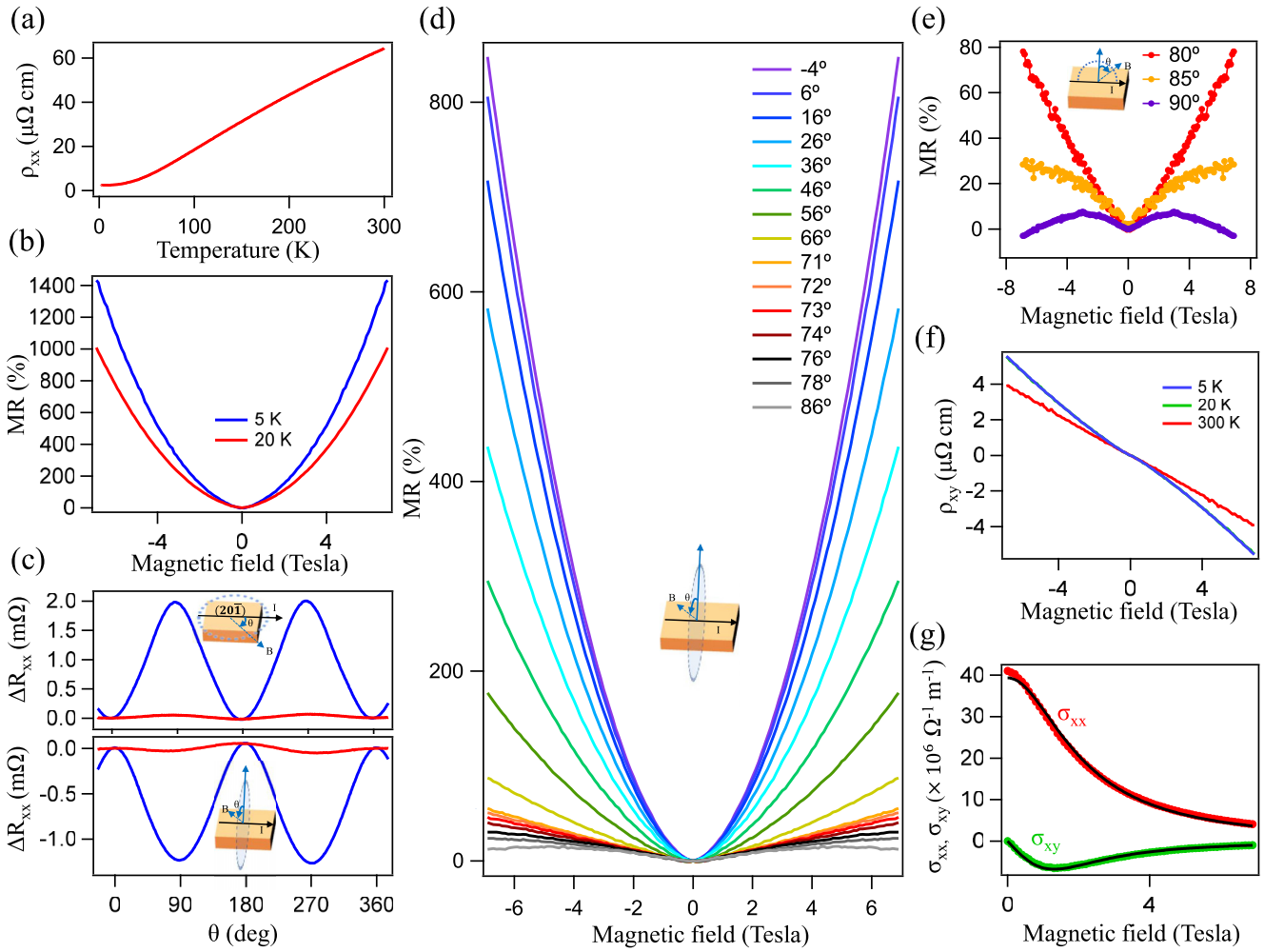


FIG. 4. (a) Temperature dependence of the longitudinal resistivity, $\rho_{xx}(T)$. (b) MR as a function of magnetic field at 5 K and 20 K. (c) Anisotropic MR $[\Delta R_{xx} = R_{xx}(\theta) - R_{xx}\ (0\ \text{deg})]$ measured at 6 T as a function of field angle θ for in-plane (top panel) and out-of-plane (bottom panel) rotations at 5 K and 300 K. The measurement geometries are demonstrated in the schematics. MR (B, θ) for field rotation in a plane oriented (d) perpendicular and (e) parallel to the current direction (b axis). (f) Hall resistivity, ρ_{xy}, versus magnetic field at three representative temperatures. (g) Longitudinal conductivity σ_{xx} and Hall conductivity σ_{xy} as a function of magnetic field at 5 K, with solid lines representing the two-band model fitting.

tionally challenging. Band structure calculations across the $TmPn_2$ family predict similar Fermi surfaces, featuring sheets near the L point and an absence of states near Γ, closely matching our observations for $TaSb_2$ [23,25]. Furthermore, ARPES data from sister compounds $NbAs_2$ and $TaAs_2$, which also cleave along the $(20\bar{1})$ plane, exhibit similar electronic profiles with multiple electron- and holelike bands crossing the Fermi level [27,37,72]. The FS maps also showcase open-orbit FSs in both of the compounds. However, unlike the bulk open-orbit FSs reported in other $TmPn_2$ compounds [36,37], the open FSs in the $(20\bar{1})$ plane of $TaSb_2$ originate from topologically protected surface states, which gives rise to the WAL in MR. These observations mark a significant step toward understanding the electronic structure and its influence on the transport properties of $TaSb_2$. In this regard, a recent study on encapsulated $TaAs_2$ nanowires demonstrated how coexisting WTI phases on the $(20\bar{1})$, (201), and (001) surfaces, together with a TCI phase on the (010) surface, give rise to very distinct transport phenomena [67], including quantum coherent surface transport. Importantly, topological surface state (TSS) transport in $TaAs_2$ nanowires persist to much higher temperatures than in typical topological semimetals, highlighting the potential of the $TmPn_2$ family for quantum nanotechnology applications.

V. CONCLUSIONS

In summary, our combined ARPES, DFT, and magnetotransport studies provide a comprehensive picture of the electronic structure of $TaSb_2$ along the weakly topological $(20\bar{1})$ plane. Comparison with DFT calculations allows us to distinguish surface states from bulk bands. Multiple electron- and holelike bulk bands cross the Fermi level, leading to near-perfect carrier compensation that gives rise to the large MR. Distinct topological surface states appear along $L - X$ and $Z - X1$. These surface states are open parallel to $L - Z$. The nontrivial topology of the WTI phase gives rise to a surface-derived band crossing point at $\bar{M}$. Dichroic ARPES with different photon energies (Sec. III in the Supplemental Material [60]) indicate possible spin-polarized nature of

these open surface states [73–75]. Consistent with these observations, magnetotransport measurements show WAL at low magnetic field range. These findings provide important insight into the interplay between bulk and topological surface states and their combined impact on the magnetotransport properties of $TaSb_2$.

ACKNOWLEDGMENTS

We thank Dr. Oleg Janson and Dr. Anumita Bose for insightful discussions. We acknowledge the beamtime provided at the 1^3-ARPES end station at BESSY II, where all ARPES measurements reported in this work were performed. The work at IFW and HZB was supported by the Deutsche Forschungsgemeinschaft under Grant SFB No. 1143 (Project No. C04) and the Würzburg-Dresden Cluster of Excellence ctd.qmat Complexity, Topology and Dynamics in Quantum Matter (EXC 2147, Project-ID 390858490). This work was performed during the research visit in the Leibniz Institute for Solid state and Materials Research, Dresden, as a part of collaboration between the Leibniz Institute for Solid state and Materials Research, Dresden, and S. N. Bose National Centre for Basic Science, Kolkata. This research has made use of the Technical Research Centre (TRC) instrument facilities of the S. N. Bose National Centre for Basic Sciences, established under the TRC project of the Department of Science and Technology (DST), Govt. of India. S.C. acknowledges the support by BMBF funding through Project No. 01DK240008 (GU-QuMat). S.T. thanks the financial support provided by UGC-DAE CSR through Grant No. CRS/2021-22/01/373. O.S. and B.B. acknowledge the support of BMBF through project "Instant micro-ARPES for in-operando tuning of material and device properties." S.T. thanks the Science and Engineering Research Board (SERB), Department of Science and Technology (DST), India, for the financial support through Grant No. SRG/2020/000393. We thank Ulrike Nitzsche for technical assistance. D.V.E. acknowledges DFG for financial support (Grants No. 529677299 and No. 449494427).

DATA AVAILABILITY

There are no publicly available research data or software supporting this manuscript. Requests for further information or data should be sent to the authors.

[1] K. v. Klitzing, G. Dorda, and M. Pepper, New method for high-accuracy determination of the fine-structure constant based on quantized Hall resistance, Phys. Rev. Lett. **45**, 494 (1980).

[2] C. L. Kane and E. J. Mele, Quantum spin Hall effect in graphene, Phys. Rev. Lett. **95**, 226801 (2005).

[3] C. L. Kane and E. J. Mele, Z_2 topological order and the quantum spin Hall effect, Phys. Rev. Lett. **95**, 146802 (2005).

[4] D. Hsieh, D. Qian, L. Wray, Y. Xia, Y. S. Hor, R. J. Cava, and M. Z. Hasan, A topological Dirac insulator in a quantum spin Hall phase, Nature (London) **452**, 970 (2008).

[5] J. E. Moore, The birth of topological insulators, Nature (London) **464**, 194 (2010).

[6] Z. Wang, Y. Sun, X.-Q. Chen, C. Franchini, G. Xu, H. Weng, X. Dai, and Z. Fang, Dirac semimetal and topological phase transitions in A_3Bi (A = Na, K, Rb), Phys. Rev. B **85**, 195320 (2012).

[7] S. Borisenko, Q. Gibson, D. Evtushinsky, V. Zabolotnyy, B. Büchner, and R. J. Cava, Experimental realization of a three-dimensional Dirac semimetal, Phys. Rev. Lett. **113**, 027603 (2014).

[8] M. Neupane, S.-Y. Xu, R. Sankar, N. Alidoust, G. Bian, C. Liu, I. Belopolski, T.-R. Chang, H.-T. Jeng, H. Lin, *et al.*, Observation of a three-dimensional topological Dirac semimetal phase in high-mobility Cd_3As_2, Nat. Commun. **5**, 3786 (2014).

[9] X. Wan, A. M. Turner, A. Vishwanath, and S. Y. Savrasov, Topological semimetal and Fermi-arc surface states in the electronic structure of pyrochlore iridates, Phys. Rev. B **83**, 205101 (2011).

[10] S.-Y. Xu, I. Belopolski, N. Alidoust, M. Neupane, G. Bian, C. Zhang, R. Sankar, G. Chang, Z. Yuan, C.-C. Lee, *et al.*, Discovery of a Weyl fermion semimetal and topological Fermi arcs, Science **349**, 613 (2015).

[11] H. Weng, C. Fang, Z. Fang, B. A. Bernevig, and X. Dai, Weyl semimetal phase in noncentrosymmetric transition-metal monophosphides, Phys. Rev. X **5**, 011029 (2015).

[12] L. Huang, T. M. McCormick, M. Ochi, Z. Zhao, M.-T. Suzuki, R. Arita, Y. Wu, D. Mou, H. Cao, J. Yan, *et al.*, Spectroscopic evidence for a type II Weyl semimetallic state in $MoTe_2$, Nat. Mater. **15**, 1155 (2016).

[13] L. Fu and C. L. Kane, Superconducting proximity effect and Majorana fermions at the surface of a topological insulator, Phys. Rev. Lett. **100**, 096407 (2008).

[14] R. M. Lutchyn, J. D. Sau, and S. D. Sarma, Majorana fermions and a topological phase transition in semiconductor-superconductor heterostructures, Phys. Rev. Lett. **105**, 077001 (2010).

[15] V. Kozii, J. W. Venderbos, and L. Fu, Three-dimensional Majorana fermions in chiral superconductors, Sci. Adv. **2**, e1601835 (2016).

[16] B. Bradlyn, J. Cano, Z. Wang, M. Vergniory, C. Felser, R. J. Cava, and B. A. Bernevig, Beyond Dirac and Weyl fermions: Unconventional quasiparticles in conventional crystals, Science **353**, aaf5037 (2016).

[17] P. Tang, Q. Zhou, and S.-C. Zhang, Multiple types of topological fermions in transition metal silicides, Phys. Rev. Lett. **119**, 206402 (2017).

[18] F. Schindler, A. M. Cook, M. G. Vergniory, Z. Wang, S. S. Parkin, B. A. Bernevig, and T. Neupert, Higher-order topological insulators, Sci. Adv. **4**, eaat0346 (2018).

[19] C. Nayak, S. H. Simon, A. Stern, M. Freedman, and S. D. Sarma, Non-Abelian anyons and topological quantum computation, Rev. Mod. Phys. **80**, 1083 (2008).

[20] A. Stern and N. H. Lindner, Topological quantum computation—from basic concepts to first experiments, Science **339**, 1179 (2013).

[21] S.-Y. Xu, N. Alidoust, I. Belopolski, Z. Yuan, G. Bian, T.-R. Chang, H. Zheng, V. N. Strocov, D. S. Sanchez, G. Chang, *et al.*, Discovery of a Weyl fermion state with Fermi arcs in niobium arsenide, Nat. Phys. **11**, 748 (2015).

[22] S.-Y. Xu, I. Belopolski, D. S. Sanchez, C. Zhang, G. Chang, C. Guo, G. Bian, Z. Yuan, H. Lu, T.-R. Chang, *et al.*, Experimental discovery of a topological Weyl semimetal state in TaP, Sci. Adv. **1**, e1501092 (2015).

[23] C. Xu, J. Chen, G.-X. Zhi, Y. Li, J. Dai, and C. Cao, Electronic structures of transition metal dipnictides XPn_2 (X = Ta, Nb; Pn = P, As, Sb), Phys. Rev. B **93**, 195106 (2016).

[24] Y. Shao, Z. Sun, Y. Wang, C. Xu, R. Sankar, A. J. Breindel, C. Cao, M. M. Fogler, A. J. Millis, F. Chou, *et al.*, Optical signatures of Dirac nodal lines in $NbAs_2$, Proc. Natl. Acad. Sci. USA **116**, 1168 (2019).

[25] B. Wang, B. Singh, B. Ghosh, W.-C. Chiu, M. M. Hosen, Q. Zhang, L. Ying, M. Neupane, A. Agarwal, H. Lin, and A. Bansil, Topological crystalline insulator state with type-II Dirac fermions in transition metal dipnictides, Phys. Rev. B **100**, 205118 (2019).

[26] X.-L. Liu, H.-Y. Wang, H. Su, Z.-H. Yu, and Y.-F. Guo, Nontrivial topological states in the tantalum dipnictides TaX_2 (X= As, P), Tungsten **2**, 251 (2020).

[27] S. Regmi, C.-Y. Huang, M. A. Khan, B. Wang, A. P. Sakhya, M. M. Hosen, J. Thompson, B. Singh, J. D. Denlinger, M. Ishigami, J. F. Mitchell, D. Kaczorowski, A. Bansil, and M. Neupane, Electronic structure in a transition metal dipnictide $TaAs_2$, J. Phys.: Condens. Matter **36**, 075502 (2024).

[28] P. Li, P. Qiu, Q. Xu, J. Luo, Y. Xiong, J. Xiao, N. Aryal, Q. Li, L. Chen, and X. Shi, Colossal Nernst power factor in topological semimetal $NbSb_2$, Nat. Commun. **13**, 7612 (2022).

[29] J.-E. Lee, Y. Liu, J. Hwang, C. Hwang, C. Petrovic, S. Y. Park, H. Ryu, and S.-K. Mo, Topological surface states of semimetal $TaSb_2$, Nano Converg. **11**, 50 (2024).

[30] S. Wu, Y. Pan, X. Wang, T. Xie, S. Zheng, Y. Liu, W. Li, Z. Zhou, B. Ruan, X. Lu, G. Wang, and X. Zhou, Dirac fermion and phonon coupling toward giant Nernst thermoelectric performance in topological semimetal $TaSb_2$, Adv. Mater. **37**, e08627 (2025).

[31] Y. Li, L. Li, J. Wang, T. Wang, X. Xu, C. Xi, C. Cao, and J. Dai, Resistivity plateau and negative magnetoresistance in the topological semimetal $TaSb_2$, Phys. Rev. B **94**, 121115 (2016).

[32] Y.-Y. Wang, Q.-H. Yu, P.-J. Guo, K. Liu, and T.-L. Xia, Resistivity plateau and extremely large magnetoresistance in $NbAs_2$ and $TaAs_2$, Phys. Rev. B **94**, 041103 (2016).

[33] L. Guo, Y.-K. Liu, G.-Y. Gao, Y.-Y. Huang, H. Gao, L. Chen, W. Zhao, W. Ren, S.-Y. Li, X.-G. Li, *et al.*, Extreme magnetoresistance and SdH oscillation in compensated semimetals of $NbSb_2$ single crystals, J. Appl. Phys. **123**, 155103 (2018).

[34] I. A. Leahy, Y.-P. Lin, P. E. Siegfried, A. C. Treglia, J. C. W. Song, R. M. Nandkishore, and M. Lee, Nonsaturating large magnetoresistance in semimetals, Proc. Natl. Acad. Sci. USA **115**, 10570 (2018).

[35] A. Pariari, R. Singha, S. Roy, B. Satpati, and P. Mandal, Anisotropic transverse magnetoresistance and Fermi surface in $TaSb_2$, Sci. Rep. **8**, 10527 (2018).

[36] R. Lou, Y. F. Xu, L.-X. Zhao, Z.-Q. Han, P.-J. Guo, M. Li, J.-C. Wang, B.-B. Fu, Z.-H. Liu, Y.-B. Huang, P. Richard, T. Qian, K. Liu, G.-F. Chen, H. M. Weng, H. Ding, and S.-C. Wang, Observation of open-orbit Fermi surface topology in the extremely large magnetoresistance semimetal $MoAs_2$, Phys. Rev. B **96**, 241106 (2017).

[37] R. Lou, Y. Wang, L. Zhao, C. Xu, M. Li, X. Chen, A. Zhang, Y. Huang, C. Cao, G. Chen, *et al.*, Electronic structure and open-orbit Fermi surface topology in isostructural semimetals $NbAs_2$ and W_2As_3 with extremely large magnetoresistance, Appl. Phys. Lett. **120**, 123101 (2022).

[38] B. Shen, X. Deng, G. Kotliar, and N. Ni, Fermi surface topology and negative longitudinal magnetoresistance observed in the semimetal $NbAs_2$, Phys. Rev. B **93**, 195119 (2016).

[39] H. Wang, H. Su, J. Zhang, W. Xia, Y. Lin, X. Liu, X. Hou, Z. Yu, N. Yu, X. Wang, Z. Zou, Y. Wang, Q. Liang, Y. Zhen, and Y. Guo, Quantum oscillations and nontrivial topological state in a compensated semimetal TaP_2, Phys. Rev. B **100**, 115127 (2019).

[40] Y. Li, C. An, C. Hua, X. Chen, Y. Zhou, Y. Zhou, R. Zhang, C. Park, Z. Wang, Y. Lu, *et al.*, Pressure-induced superconductivity in topological semimetal $NbAs_2$, npj Quantum Mater. **3**, 58 (2018).

[41] M.-D. Zhang, X.-Y. Hou, Q. Wang, Y.-Y. Wang, L.-X. Zhao, Z. Wang, Y.-D. Gu, F. Zhang, T.-L. Xia, Z.-A. Ren, G.-F. Chen, N. Hao, and L. Shan, Tip-induced superconductivity on the topological semimetals $TaAs_2$ and $NbAs_2$, Phys. Rev. B **102**, 085139 (2020).

[42] L. Fu and C. L. Kane, Topological insulators with inversion symmetry, Phys. Rev. B **76**, 045302 (2007).

[43] M. Z. Hasan and C. L. Kane, *Colloquium*: Topological insulators, Rev. Mod. Phys. **82**, 3045 (2010).

[44] C. Pauly, B. Rasche, K. Koepernik, M. Richter, S. Borisenko, M. Liebmann, M. Ruck, J. van den Brink, and M. Morgenstern, Electronic structure of the dark surface of the weak topological insulator $Bi_{14}Rh_3I_9$, ACS Nano **10**, 3995 (2016).

[45] J. Kruthoff, J. de Boer, J. van Wezel, C. L. Kane, and R.-J. Slager, Topological classification of crystalline insulators through band structure combinatorics, Phys. Rev. X **7**, 041069 (2017).

[46] Z. Song, T. Zhang, Z. Fang, and C. Fang, Quantitative mappings between symmetry and topology in solids, Nat. Commun. **9**, 3530 (2018).

[47] Z. Cao, F. Tang, D. Wang, and X. Wan, First-principles identification of topological crystalline insulators with C_2 rotation anomaly, Phys. Rev. B **103**, 155113 (2021).

[48] M. Eschbach, M. Lanius, C. Niu, E. Młyńczak, P. Gospodarič, J. Kellner, P. Schüffelgen, M. Gehlmann, S. Döring, E. Neumann, *et al.*, Bi_1Te_1 is a dual topological insulator, Nat. Commun. **8**, 14976 (2017).

[49] N. Avraham, A. Kumar Nayak, A. Steinbok, A. Norris, H. Fu, Y. Sun, Y. Qi, L. Pan, A. Isaeva, A. Zeugner, *et al.*, Visualizing coexisting surface states in the weak and crystalline topological insulator Bi_2TeI, Nat. Mater. **19**, 610 (2020).

[50] D.-Y. Wang, Q. Jiang, K. Kuroda, K. Kawaguchi, A. Harasawa, K. Yaji, A. Ernst, H.-J. Qian, W.-J. Liu, H.-M. Zha, Z.-C. Jiang, N. Ma, H.-P. Mei, A. Li, T. Kondo, S. Qiao, and M. Ye, Coexistence of strong and weak topological orders in a quasi-one-dimensional material, Phys. Rev. Lett. **129**, 146401 (2022).

[51] M. Brahlek, Criteria for realizing room-temperature electrical transport applications of topological materials, Adv. Mater. **32**, 2005698 (2020).

[52] M. J. Gilbert, Topological electronics, Commun. Phys. **4**, 70 (2021).

[53] FPLO, https://www.fplo.de/.

[54] K. Koepernik and H. Eschrig, Full-potential nonorthogonal local-orbital minimum-basis band-structure scheme, Phys. Rev. B **59**, 1743 (1999).

[55] J. P. Perdew, K. Burke, and M. Ernzerhof, Generalized gradient approximation made simple, Phys. Rev. Lett. **77**, 3865 (1996).

[56] F. Hulliger, New representatives of the $NbAs_2$ and $ZrAs_2$ structures, Nature (London) **204**, 775 (1964).

[57] FIZ Karlsruhe, Inorganic crystal structure database (ICSD), entry 651600 (1964), https://www.fiz-karlsruhe.de/en/produkte-und-dienstleistungen/inorganic-crystal-structure-database-icsd.

[58] M. P. L. Sancho, J. M. L. Sancho, J. M. L. Sancho, and J. Rubio, Highly convergent schemes for the calculation of bulk and surface Green functions, J. Phys. F **15**, 851 (1985).

[59] V. Antonov, B. Harmon, and A. Yaresko, *Electronic Structure and Magneto-Optical Properties of Solids* (Kluwer Academic Publishers, Dordrecht, Boston, London, 2004).

[60] See Supplemental Material at http://link.aps.org/supplemental/10.1103/9gk1-krjp for contains the calculation of Z_2 topological invariant from the parity eigenvalues in Sec. I. Section II and Fig S2 showcase Dirac surface states sitting right at the TRIM $\bar{M}$ at ∼–0.6 eV below Fermi level. Section III focuses on the circular dichroism at different photon energies along with the measurement geometry, which includes Refs. [23,25,42,61–63,73–75].

[61] K. Lee, G. F. Lange, L.-L. Wang, B. Kuthanazhi, T. V. Trevisan, N. H. Jo, B. Schrunk, P. P. Orth, R.-J. Slager, P. C. Canfield, *et al.*, Discovery of a weak topological insulating state and van Hove singularity in triclinic $RhBi_2$, Nat. Commun. **12**, 1855 (2021).

[62] R. Noguchi, T. Takahashi, K. Kuroda, M. Ochi, T. Shirasawa, M. Sakano, C. Bareille, M. Nakayama, M. Watson, K. Yaji, *et al.*, A weak topological insulator state in quasi-one-dimensional bismuth iodide, Nature (London) **566**, 518 (2019).

[63] P. Zhang, R. Noguchi, K. Kuroda, C. Lin, K. Kawaguchi, K. Yaji, A. Harasawa, M. Lippmaa, S. Nie, H. Weng, *et al.*, Observation and control of the weak topological insulator state in $ZrTe_5$, Nat. Commun. **12**, 406 (2021).

[64] R. Singha, A. Pariari, G. K. Gupta, T. Das, and P. Mandal, Probing the Fermi surface and magnetotransport properties of $MoAs_2$, Phys. Rev. B **97**, 155120 (2018).

[65] X. Sun, F. Tang, X. Shen, W. Sun, W. Zhao, Y. Han, X. Kan, S. Cong, L. Zhang, Z. Han, B. Qian, X. Jiang, S. Wang, R. Zheng, and Y. Fang, Anisotropic giant magnetoresistance and Fermi surface topology in the layered compound $YbBi_2$, Phys. Rev. B **105**, 195114 (2022).

[66] J. Bannies, E. Razzoli, M. Michiardi, H.-H. Kung, I. S. Elfimov, M. Yao, A. Fedorov, J. Fink, C. Jozwiak, A. Bostwick, E. Rotenberg, A. Damascelli, and C. Felser, Extremely large magnetoresistance from electron-hole compensation in the nodal-loop semimetal ZrP_2, Phys. Rev. B **103**, 155144 (2021).

[67] A. Roy, A. Eyal, R. Majlin Skiff, B. Barick, S. D. Escribano, O. Brontvein, K. Rechav, O. Bitton, R. Ilan, and E. Joselevich, Intertwined topological phases in $TaAs_2$ nanowires with giant magnetoresistance and quantum coherent surface transport, Adv. Mater. **37**, 2418279 (2025).

[68] X. Huang, L. Zhao, Y. Long, P. Wang, D. Chen, Z. Yang, H. Liang, M. Xue, H. Weng, Z. Fang, X. Dai, and G. Chen, Observation of the chiral-anomaly-induced negative magnetoresistance in 3D Weyl semimetal TaAs, Phys. Rev. X **5**, 031023 (2015).

[69] Y.-F. Huang, W.-L. Zhu, Y.-Y. Wang, Q.-X. Dong, L.-B. Zhang, C.-S. Li, H. OuYang, Z.-A. Ren, and G.-F. Chen, Large unsaturated transverse and negative longitudinal magnetoresistance in the compensated semimetal $MoGe_2$, Phys. Rev. B **103**, 134116 (2021).

[70] Z. Li, Y. Zeng, J. Zhang, M. Zhou, and W. Wu, Observation of negative longitudinal magnetoresistance in the type-II Dirac semimetal $PtSe_2$, Phys. Rev. B **98**, 165441 (2018).

[71] L.-K. Zeng, R. Lou, D.-S. Wu, Q. N. Xu, P.-J. Guo, L.-Y. Kong, Y.-G. Zhong, J.-Z. Ma, B.-B. Fu, P. Richard, P. Wang, G. T. Liu, L. Lu, Y.-B. Huang, C. Fang, S.-S. Sun, Q. Wang, L. Wang, Y.-G. Shi, H. M. Weng, *et al.*, Compensated semimetal LaSb with unsaturated magnetoresistance, Phys. Rev. Lett. **117**, 127204 (2016).

[72] A. S. Wadge, G. Grabecki, C. Autieri, B. J. Kowalski, P. Iwanowski, G. Cuono, M. F. Islam, C. M. Canali, K. Dybko, A. Hruban, A. Łusakowski, T. Wojciechowski, R. Diduszko, A. Lynnyk, N. Olszowska, M. Rosmus, J. Kołodziej, and A. Wiśniewski, Electronic properties of $TaAs_2$ topological semimetal investigated by transport and ARPES, J. Phys.: Condens. Matter **34**, 125601 (2022).

[73] S. R. Park, C. H. Kim, J. Yu, J. H. Han, and C. Kim, Orbital-angular-momentum based origin of Rashba-type surface band splitting, Phys. Rev. Lett. **107**, 156803 (2011).

[74] J.-H. Park, C. H. Kim, J.-W. Rhim, and J. H. Han, Orbital Rashba effect and its detection by circular dichroism angle-resolved photoemission spectroscopy, Phys. Rev. B **85**, 195401 (2012).

[75] Y. Wang and N. Gedik, Circular dichroism in angle-resolved photoemission spectroscopy of topological insulators, Phys. Status Solidi RRL **7**, 64 (2013).